Violation of centrosymmetry in time-resolved ultrafast-electron diffraction from vibrating oriented diatomic molecules

Hua-Chieh Shao and Anthony F. Starace

Phys. Rev. A **101**, 022704 — Published 14 February 2020

DOI: 10.1103/PhysRevA.101.022704

Violation of centrosymmetry in time-resolved ultrafast electron diffraction from vibrating oriented diatomic molecules

Hua-Chieh Shao and Anthony F. Starace*
Department of Physics and Astronomy, The University of Nebraska, Lincoln, Nebraska 68588-0299, USA
(Dated: January 16, 2020)

Violation of centrosymmetry (VOC) in time-resolved diffraction patterns has been predicted in ultrafast electron and x-ray diffraction from electronic and molecular motions. Extending from our x-ray studies, we theoretically investigate the VOC in time-resolved ultrafast electron diffraction (UED) from ro-vibrational motion of oriented diatomic molecules lithium hydride and hydrogen. We simulate and compare the electron and x-ray diffraction images, especially focused on the differences in the VOC and molecular interference fringes. In addition, using Newton diagrams, we provide an intuitive semi-classical interpretation to explain how the VOC is arisen from and related to the particles' motion and why is there an anticorrelation between the VOC and molecular interference fringes.

I. INTRODUCTION

A thorough understanding of the chemical or biological functions of a molecule in reactions necessitates knowledge of the connection between its structure and the reaction dynamics [1, 2]. Direct imaging of transient molecular structures in real time, therefore, renders valuable insight into underlying reaction mechanisms, thus allowing one to possibly control them. However, imaging molecular motion demands stringent spatial and temporal resolution. Due to their short wavelengths, ultrafast electrons and x rays are frequently employed as probes to investigate structural dynamics with atomic precision [3–7]. In recent years there has been steady progress on improving temporal resolutions in ultrafast electron diffraction [8–10] and microscopy [11–14]. In particular, novel schemes and designs have been demonstrated to accelerate, manipulate, and compress electron pulses with energies ranging from keV to MeV using dielectric laser accelerators [15–19], radio-frequency cavities [20–24], terahertz radiation [25–28], and optical gating [29, 30]. Owing to these advances, time-resolved structural dynamics in various systems have been studied using laser pump-electron probe schemes, such as in photoinduced unimolecular reactions [31, 32] and in phase transitions and lattice dynamics in condensed materials [33–40]. In addition to these experimental advances, theoretical models have been developed for time-dependent coherent diffraction of ultrafast electrons [41–43] and x rays [44–47], and simulations have been performed for the diffraction images of time-varying electronic and molecular motions.

In contrast to time-independent coherent diffraction, simulations of time-resolved electron and x-ray diffraction predict a distinctive feature of non-resonant diffraction images of electronic [41, 43, 45, 48–50] or molecular [47] motions: asymmetric angular distributions. In the first-order perturbation theory of time-independent ultrafast electron diffraction (UED) from a molecule, the elastic scattering amplitude is proportional to the Fourier transform of the molecular charge density $\rho(\boldsymbol{x})$ (which includes both the nuclear and electron charges),

$$F(\boldsymbol{s}) \propto \int d\boldsymbol{x}\, e^{i\boldsymbol{s}\cdot\boldsymbol{x}}\, \rho(\boldsymbol{x})\,, \tag{1}$$

where $\boldsymbol{s}$ is the momentum transfer. Since $F(-\boldsymbol{s}) = F^*(\boldsymbol{s})$ and the differential cross section is the absolute square of the scattering amplitude, $d\sigma/d\Omega = |F(\boldsymbol{s})|^2$, the angular distribution of the scattered electrons is always centrosymmetric (*i.e.*, there exists an inversion center in the diffraction image) even though the charge density may lack any symmetry. This property is called Friedel's law in crystallography [51]. As long as the density interpretation (1) is adopted, centrosymmetry holds whether or not the charge density $\rho(\boldsymbol{x})$ depends on time. Therefore, violation of centrosymmetry (VOC) indicates that the time-resolved diffraction images carry additional structural information that cannot be interpreted in terms of a charge-density formulation (1).

In previous x-ray studies [45, 47–50] the VOC asymmetries are exclusively attributed to electron motions in atoms or molecules since the Thomson scattering cross sections for nuclei are much smaller than those for electrons. In previous studies of ultrafast electron diffraction (UED) [41, 43] the focus was on the electronic motions in atoms with the nuclei treated as quasi-stationary even though both nuclei and electrons contribute to the scattering cross sections. Thus, it is unclear how the VOC is altered by scattering from nuclei when both electrons and nuclei are in motion since the corresponding scattering amplitudes depend differently on the momentum transfer $\boldsymbol{s}$. Furthermore, in studies of electronic motion in atoms [42, 43] the asymmetry was attributed to the asymmetric momentum-density distributions of the electron wiggling motions. The sign of the asymmetry (indicating the direction into which the incident electrons have higher probability to be scattered) reflects the direction of the mean momentum of the asymmetric momentum distribution. However, in a recent study of molecular motion [47] in which the center of mass of the molecule was assumed to be quasi-stationary, even

* Deceased

though the sum of the momenta of the two atoms was thus set zero, nevertheless VOC was found to still occur owing to ro-vibrational molecular motion. Moreover, as will be shown and discussed in Sec. III B, the VOC asymmetry shows a somewhat unpredictable behavior: it exhibits opposite signs (*i.e.*, opposite directions into which more electrons are scattered) for homonuclear and heteronuclear diatomic molecules having the same angular orientation. Further studies of the nature of VOC are thus necessary to understand how the VOC relates to the particle motions, in order that one can better utilize this phenomenon to interpret time-resolved diffraction images.

In this paper we have performed simulations for UED from the same diatomic molecular systems as in our recent x-ray study [47]. The schematic setup for our time-resolved UED from diatomic molecules undergoing ro-vibrational motion is shown in Fig. 1. The molecular motion is assumed to be initiated by some pump procedure that impulsively excites an electron of the molecule from the ground state to some excited state such that the nuclei maintain their states of motion (which may be pre-oriented) during the pumping process (*i.e.*, we employ the Franck-Condon principle [52]). Then the ensuing ro-vibrational motion in the excited electronic state is probed by time-delayed ultrafast electron pulses. In order to perform the molecular simulations, we generalize the UED model used for atomic systems and present the theory and our simulation details in Sec. II. In Sec. III we then apply our model to two diatomic molecular systems, lithium hydride and hydrogen, and examine the characteristics of the time-resolved UED images that reflect the ro-vibrational motion. In particular, we compare UED and x-ray diffraction scattering patterns to elucidate how the VOC and the interference fringes change when one employs the two different probes. In Sec. IV, we provide and discuss an intuitive semi-classical interpretation, with the help of Newton diagrams, to explain how the VOC and interference fringes arise naturally from kinematic relations in an electron-molecule collision and from the wave properties of the particles. Finally, in Sec. V we summarize our results and present our conclusions. We also briefly discuss the feasibility of producing an anisotropic nuclear motion which is necessary for the VOC observed in the simulations.

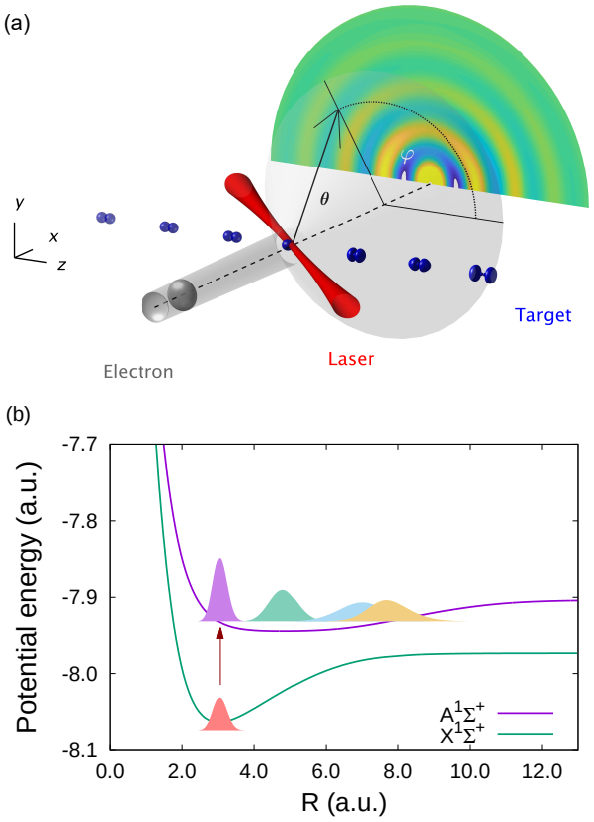

FIG. 1. Schematic setup (a) for time-resolved ultrafast electron diffraction (UED) from diatomic molecules undergoing ro-vibrational motion. An oriented molecule undergoes a vertical transition (b) from its ground electronic state to some excited state by means of a pump laser pulse. The ensuing molecular motion in the excited state is probed by a time-delayed ultrafast electron pulse with a detector recording the diffraction pattern of the scattered electrons. By varying the pump-probe delay, a series of time-resolved diffraction images reveals the molecular motion. The molecular potential energy curves of lithium hydride for the $X^1\Sigma^+$ and $A^1\Sigma^+$ states as a function of internuclear distance R are shown in (b). For future reference, the scattering angles θ and φ and the coordinate system are defined in (a).

II. THEORY AND SIMULATION

The theory of time-resolved UED has been developed in Refs. [41–43] for the purpose of imaging electronic motions in atoms. Generalization of the atomic formulation to molecular cases is conceptually straightforward (although computationally challenging): the electronic state of an atomic target is replaced by that of a molecular target. An analogous model for time-dependent coherent x-ray diffraction has been developed recently [47]. Since the technical aspects of the derivations and assumptions have been detailed in our prior publications, in the following sections we summarize the basic ideas and major assumptions of our model and refer readers to Refs. [41–43, 47] for specific details. After outlining the general theory, we then present the parameters and further assumptions specific to the molecular systems in the present simulations. Unless specified otherwise, atomic units (a.u.) are used throughout this paper.

A. Time-dependent scattering from vibrating diatomic molecules

Consider time-resolved UED from a diatomic molecule undergoing ro-vibrational motion:

$$e^-(\boldsymbol{k}_0) + M^*(\boldsymbol{k}_1) \to e^-(\boldsymbol{k}_a) + M^*(\boldsymbol{k}_b)\,. \qquad (2)$$

Here $\boldsymbol{k}_0$ and $\boldsymbol{k}_a$ ($\boldsymbol{k}_1$ and $\boldsymbol{k}_b$) are the respective momenta of the incident and scattered electrons (molecules). In order to properly describe this time-dependent scattering, the incident electrons and molecules are modeled as wave packets localized in space and time, so that their center-of-mass motions, the moment of collision, and the temporal resolution can be well defined. The localization of the wave packets is attained by *wave-packet integrals* that coherently superpose plane-wave basis states with momentum space probability amplitudes. The momentum amplitude $a_0(\boldsymbol{k}_0)$ of the incident electron pulse is modeled as a Gaussian distribution centered at the average momentum of the pulse. The longitudinal width of the momentum density $|a_0(\boldsymbol{k}_0)|^2$ is determined by the duration of the electron pulse. We further assume that the electron wave packet is transform limited [*i.e.*, no chirp in the momentum amplitude $a_0(\boldsymbol{k}_0)$] at the moment of collision, as pulse-compression techniques can be used to offset the dispersion of the pulse that occurs during its propagation toward the molecular target. The molecular wave function can be factorized into external and internal parts, *i.e.*, for the center-of-mass and the ro-vibrational motions respectively. For the external part, the momentum amplitude $a_1(\boldsymbol{k}_1)$ of the molecular wave packet is assumed to be quasi-stationary and localized in space, owing to the slow thermal motion of the heavy molecule. For the internal part, because of the impulsive excitation, the time zero of the ro-vibrational motion is well defined, provided that the time scale of the nuclear motion is much longer than that of the pump procedure. Therefore, the internal molecular state can be approximated as a coherent superposition of molecular eigenstates, with the amplitudes determined by the Franck-Condon factors for this excitation.

Based upon the above considerations, the entrance state of the scattering system (2) satisfying the initial conditions may be written as

$$\psi_{\rm coh}^{(+)} = \int d\boldsymbol{k}_0\, d\boldsymbol{k}_1\, a_0(\boldsymbol{k}_0)\, a_1(\boldsymbol{k}_1) \sum_n C_n\, \psi_i^{(+)}\,, \qquad (3)$$

where $\psi_i^{(+)}$ is a scattering state labeled by an index of the entrance channel $i = \{\boldsymbol{k}_0, \boldsymbol{k}_1, n\}$, where the quantum number n denotes symbolically the internal molecular eigenstate (*i.e.*, the collection of electronic, rotational, and vibrational quantum numbers), and C_n is the corresponding amplitude of the state n. The first part of Eq. (3) (before the summation over n) comprises the two wave-packet integrals representing the center-of-mass motions of the electron and the molecule; the second part describes the molecular ro-vibrational motion. Note that the incident electron pulses for different pump-probe delays are modeled by the same amplitude $a_0(\boldsymbol{k}_0)$; thus the dependence of the entrance state on the time delay (*i.e.*, the time between the creation of the molecular motion and the arrival of the incident electron pulse) resides in the phase of the amplitudes C_n of the ro-vibrational motion [*cf.* Eq. (31) of Ref. [41]]. The scattering state can be expressed in terms of the asymptotic state ψ_i of the entrance channel i and the electron-molecule interaction V [53],

$$\psi_i^{(+)} = \psi_i + G^{(+)}(\varepsilon_i)\, V\, \psi_i^{(+)}\,, \qquad (4)$$

where $G^{(+)}(\varepsilon_i)$ is the interaction-free Green's function with entrance channel energy ε_i, and V comprises the Coulomb interactions between the incident electron and the charged particles in the molecular target. The superscript $(+)$ indicates that the scattering state satisfies the outgoing-wave boundary condition.

B. Transition amplitude and the ensemble-averaged scattering probability (EASP)

After constructing the entrance state (3) for the incident electron and molecule, the wave packets are then propagated in time, and the transition amplitudes at different time delays are calculated. The transition amplitude from the initial state to a final state $f \neq i$ is the projection

$$\mathscr{A}_f \equiv \lim_{t\to\infty} \left(\psi_f(t), \psi_{\rm coh}^{(+)}(t)\right)\,, \qquad (5)$$

where ψ_f is the asymptotic state of the exit channel $f = \{\boldsymbol{k}_a, \boldsymbol{k}_b, m\}$ with energy ε_f. Substituting Eq. (3), together with Eq. (4), into Eq. (5), the transition amplitude can be evaluated. In order to simplify the calculation, we make the following assumptions. In typical UED experiments, the kinetic energies of the electron pulses range from tens of keV to a few MeV, so the first-order Born approximation is adequate to evaluate the transition matrix element,

$$\mathscr{T}_{fi} \equiv (\psi_f, V\, \psi_i^{(+)}), \qquad (6)$$

for molecular targets comprised of light atoms. For the same reason, exchange effects between the incident electron and the molecular electrons are neglected. Details concerning the evaluation of $\mathscr{T}_{fi}$ can be found in the discussion following Eq. (32) in Ref. [41]. In brief, since the entrance state (3) is a coherent superposition state, the transition amplitude,

$$\mathscr{A}_f = \sum_n C_n \int d\boldsymbol{k}_0\, d\boldsymbol{k}_1\, a_0(\boldsymbol{k}_0)\, a_1(\boldsymbol{k}_1)\, 2\pi\, \delta(\varepsilon_f - \varepsilon_i)\, \mathscr{T}_{fi}, \qquad (7)$$

is a coherent sum of the transition matrix elements $\mathscr{T}_{fi}$ for all components in the entrance state i to the final state ψ_f, weighted by their corresponding amplitudes a_0, a_1, and C_n and satisfying the conservation of energy component-wise. Here, $\delta(\cdot)$ is the Dirac δ function representing the conservation of energy.

The scattering probability involves an integration and sum of the transition density $|\mathscr{A}_f|^2$ over exit channels

$f = \{\boldsymbol{k}_a, \boldsymbol{k}_b, m\}$,

$$\mathscr{P} = \sum_m \int d\boldsymbol{k}_a \, d\boldsymbol{k}_b \, |\mathscr{A}_f|^2 \,, \tag{8}$$

where the ranges of the incoherent final-state sum and the momentum integrals depend on the unresolved exit channels in diffraction measurements. We assume that only the scattering angles θ and φ of the incident electrons are measured [see Fig. 1 for definitions of these angles]. Thus, unresolved channels, such as elastic ($m = n$) and inelastic ($m \neq n$) transitions, the final momentum $\boldsymbol{k}_b$ of the molecule, and the kinetic energy of the scattered electron, are summed. In addition, the target gas is considered to be an ensemble of molecules randomly positioned in space, for controlling the positions of molecules with atomic precision remains a challenge in gas-phase scattering. Therefore, the scattering probability (8) must be further averaged over all possible positions of the molecular targets,

$$\langle \mathscr{P} \rangle = E[\mathscr{P}(\boldsymbol{b})] \,, \tag{9}$$

where $E[\,\cdot\,]$ stands for the expectation value, and $\boldsymbol{b}$ is a random variable for the position of a molecular target. We assume that the molecular gas ensemble is homogeneous in its transverse direction (with respect to the propagation direction of the incident electrons) with a dimension much larger than the cross section of the incident electron pulse. However, its longitudinal dimension is assumed to be narrow in order to avoid loss of temporal resolution due to group velocity mismatch between the pump laser and the probe electron pulses propagating through the gas ensemble. The effect of velocity mismatch can be further mitigated using tilted optical or electron pulses [54, 55] or relativistic electron pulses [21, 22], so this effect is neglected in our model. For the details of the ensemble average, see the discussions of Eqs. (28), (30), and (31) in Ref. [43]. The ensemble-averaged scattering probability (EASP) is the principal equation used to simulate the time-resolved diffraction images in this paper.

In order to understand how the scattering probability (8) describes the delay dependence and governs the temporal resolution in time-resolved measurements, we provide the following observations and analysis. The entrance state (3) is a wave packet coherently superposing multiple momentum and energy components, and the information on the delay dependence is carried by the amplitudes C_n. As the collision induces transitions from the components $\psi_i^{(+)}$ of $\psi_{\rm coh}^{(+)}$ to a final state ψ_f, these transitions $\mathscr{T}_{fi}$, weighted by their amplitudes a_0, a_1, and C_n, can interfere with each other in the scattering probability, yielding a time delay dependence that reflects the molecular motion. The interference of two transitions to the same final state requires also that the conservation laws of momentum and energy are satisfied. As a result, the energy difference between two molecular eigenstates has to be counterbalanced by two momentum components of the electron pulse having the same energy difference. A large energy difference between the molecular eigenstates (*i.e.*, corresponding to a fast quantum beat) sets the minimum bandwidth of a pulse for such interference to occur, which in turn, according to Heisenberg's uncertainty relation, determines the maximum pulse duration and temporal resolution of the time-resolved measurement.

Having thus presented our theoretical framework, in what follows we provide details concerning our simulations of UED from oriented diatomic molecules undergoing ro-vibrational motion.

C. Calculation of transition matrix elements

As shown in Eq. (7), calculation of the transition amplitudes $\mathscr{A}_f$ requires knowledge of the transition matrix elements $\mathscr{T}_{fi}$. In the first-order Born approximation, the transition matrix elements are approximated by $\mathscr{T}_{fi} \simeq (\psi_f, V\,\psi_i)$. Thus, the first step in calculating $\mathscr{T}_{fi}$ is to determine the eigenstates of the molecular target. We employ the Born-Oppenheimer approximation, so the eigenstates factorize into electronic and nuclear parts. The electronic energies as a function of internuclear distance (*i.e.*, the molecular potential energy curves) are obtained from the literature or from quantum chemistry simulations. The vibrational wave functions are calculated using these potential energy curves and a Fourier grid Hamiltonian method [56].

As our focus is on the VOC induced by the nuclear motion, we assume that the quantum beat motion of the electron excited by the pump pulse is so fast such that it cannot be resolved by the electron pulse. As a result, the overall scattering probability is an incoherent sum of the scattering probabilities from the excited and ground electronic states, and the information of the correlation between the electronic states is lost in the measurement [see, *e.g.*, Ref. [43]]. In addition, under the Born approximation where the scattering mechanism is simple, inelastic electronic transitions seem unlikely to alter the features in diffraction patterns significantly. Furthermore, we note that the inelastic electronic transitions peak in the forward direction for UED [57] and their contributions can be reduced by energy-resolved measurements. Therefore, we do not include these transitions. The distortion of the valence electron density due to the binding force is also neglected. Thus, the elastic scatterings from the molecular electronic states are approximated using atomic form factors [see also the discussions of Eqs. (41) and (42) in Ref. [47]]. The atomic form factors are obtained from Ref. [58]. Note finally that although molecular electronic transitions are neglected, transitions among the ro-vibrational molecular states are included in calculating the transition amplitudes.

The transition matrix elements for UED from a di-

atomic molecule are thus approximated as

$$\mathscr{T}_{fi} \simeq \delta(\mathcal{P}_f - \mathcal{P}_i) \sum_{j=1}^{2} \frac{1}{2\pi^2} \frac{1}{s^2} \big(- Z_j + f_j(s) \big) \times \int d\boldsymbol{R}\, e^{i\boldsymbol{s}\cdot\boldsymbol{R}_j}\, \phi_m^*\, \phi_n \,, \tag{10}$$

where $\mathcal{P}_f = \boldsymbol{k}_a + \boldsymbol{k}_b$ and $\mathcal{P}_i = \boldsymbol{k}_0 + \boldsymbol{k}_1$ are the respective total linear momenta of the exit and entrance channels, $\delta(\cdot)$ is the Dirac δ function representing the conservation of momentum, $\boldsymbol{s} = \boldsymbol{k}_0 - \boldsymbol{k}_a$ is the momentum transfer during the collision, Z_j is the nuclear charge of the jth atom in the molecule, $f_j(s)$ is the atomic form factor, $\boldsymbol{R}$ is the internuclear distance, $\boldsymbol{R}_j$ is the position vector of the jth atom in the molecular reference frame, and ϕ_m and ϕ_n are the respective final and initial nuclear eigenstates. We have also used the fact that the mass of a nucleus is much larger than that of an electron. The expression after the j-summation in the first line of Eq. (10) is the *atomic scattering amplitude* from the jth atom, and the second line is the transition amplitude for the nuclear state (*i.e.*, the ro-vibrational state) in which information on the molecular structure is embedded. In other words, $\mathscr{T}_{fi}$ is approximated as a coherent sum of the scattering amplitudes from the constituent atoms in a molecule weighted by the amplitude of the $n \to m$ nuclear transition and it satisfies the conservation of linear momentum.

D. Wave-packet amplitudes

Having calculated the transition matrix elements (10), the wave-packet integrals in Eq. (7) can be performed to obtain the transition amplitude. To proceed, we must specify the amplitudes a_0, a_1, and C_n. The electron pulses are assumed to be axially symmetric and well collimated, so the transverse width of the momentum amplitude $a_0(\boldsymbol{k}_0)$ is small and thus $\mathscr{T}_{fi}$ is insensitive to integration over the transverse momenta in the wave-packet integrals. Hence, the transverse momentum components of $\boldsymbol{k}_0$ in $\mathscr{T}_{fi}$ are approximated to be zero and the corresponding momentum integrals are calculated analytically. The momentum amplitude in the longitudinal direction is of the form $a_0(k_0) \propto e^{-(k_0-p_0)^2/2\sigma_0^2}$, where p_0 is the central momentum and σ_0 is the Gaussian width. The central kinetic energy of the incident electron pulse is 10.0 keV ($p_0 \approx 27.1$ a.u.), and the full-width-at-half-maximum (FWHM) duration of the pulse is 1.0 fs ($\sigma_0 \approx 7.4 \times 10^{-4}$ a.u.). The longitudinal momentum integral is calculated numerically using a Gauss-Hermite quadrature. The transition matrix is also assumed to be insensitive to variation of the momentum $\boldsymbol{k}_1$ of the molecule, so the $\boldsymbol{k}_1$-integral is calculated analytically.

As aforementioned, the vibrational amplitudes of the nuclear state C_n are determined by the Franck-Condon factors of the excitation, which can be found in Figs. 1 and 5 of Ref. [47]. In addition, we assume the molecules are oriented in such a way that two-thirds of the excited population is in the rotational state $J_i = 0$ and the remainder of the excited population is in the state $J_i = 1$, with $M_i = 0$ for both values of J_i. The reasons for choosing such rotational state are to acquire an oriented molecule with minimum populated rotational levels to ease the computation but still yield a reasonable degree of orientation. The rotational state gives an orientation with $\langle \cos\theta_{\mathrm{mol}} \rangle \approx 0.54$, which is achievable as shown in the simulations [59–61].

E. Molecular scattering intensity

The EASPs as functions of scattering angles θ and φ are calculated using Eq. (8) by summing all unresolved exit channels and averaging over the molecular ensemble. The final-state sum in Eq. (8) includes all molecular ro-vibrational states. In order to ease the computation, we further assume that $\mathscr{T}_{fi}$ is insensitive to the rotational quantum number J_f of the final state ϕ_m, so the closure relation for the rotational state of ϕ_m can be used. The ranges of summation for the final vibrational and rotational quantum numbers depend on the molecule and the momentum transfer. Typical ranges of the vibrational and rotational transitions in our simulations are $\Delta v \leq 40$ and $\Delta J \leq 50$, respectively. The scattering intensities from the pre-oriented molecular ground state are neglected, for it behaves like a stationary state in our model as a consequence of the impulsive excitation and the negligence of inelastic electronic transitions.

Since we are concerned with time-resolved imaging of molecular motion, the diffraction images presented in Sec. III below are EASPs that are processed to accentuate features associated with the molecular geometry. The following procedures are used to calculate the *molecular scattering intensity*, which is similar to modified molecular scattering intensities presented by others (*e.g.*, Refs. [62, 63]). The terms in the scattering probability $\mathscr{P}$ can be categorized according whether they stem from individual atoms (*atomic scattering*) or from the interference of transition amplitudes from two different atoms (*molecular scattering*). The atomic scatterings give no information about the molecular structure and are removed from our EASPs. For a diatomic molecule, this term's contribution is given approximately by $s^{-4}(|-Z_1+f_1(s)|^2 + |-Z_2+f_2(s)|^2)$, where the momentum transfer is approximated using the result for elastic scattering:

$$s = 2\, p_0 \sin(\theta/2). \tag{11}$$

To remove the contribution of this term to our EASPs, we use the following procedure. For each pump-probe delay, the two-dimensional diffraction image is reduced to a one-dimensional one by integrating over the azimuthal scattering angle φ (see Fig. 1). Then that reduced scattering probability is fitted to

$s^{-4}(|-Z_1+f_1(s)|^2+|-Z_2+f_2(s)|^2)$ to obtain a proportionality factor. The proportionality factors for all delays are averaged, and this averaged proportionality factor is used to remove a baseline of the atomic scattering contributions from all two-dimensional diffraction images. Finally, to compensate for the decrease of the scattering intensities at large scattering angles θ, these baseline-removed diffraction images are further divided by the factor $s^{-4}\,(-Z_1+f_1(s))\,(-Z_2+f_2(s))$.

III. TIME-RESOLVED UED FROM DIATOMIC MOLECULES IN RO-VIBRATIONAL MOTION

We have found that the VOC effect stemming from the ro-vibrational motion of diatomic molecules is most significant in diatomic molecules that involve the hydrogen atom. This is because of the large amplitudes of such motions when one of the atomic components is a light atom, with the H atom being the lightest of all. In this section we present results for two types of diatomic molecules in order to illustrate character of the VOC effect in time-resolved UED. The first one is a heteronuclear molecule, lithium hydride. The second one, the homonuclear hydrogen molecule in which one of the atoms is an isotope of the hydrogen atom, demonstrates that the VOC can also be observed in that case.

A. Deuterated lithium hydride molecule

The oriented ro-vibrational motion of deuterated lithium hydride (LiD) in the excited $A^1\Sigma^+$ state as a function of time is presented in the right column of Fig. 2, which shows the weighted molecular density in the yz plane perpendicular to the propagation direction of the electron pulses (see Fig. 1 for the definition of the coordinate system). The potential energy curves, taken from Ref. [64], are shown in Fig. 1(b). Deuterium is used to increase the period of the vibration and to better localize the molecular wave packet. The molecular densities in right column of Fig. 2 are weighted by the square of the internuclear distance, $\boldsymbol{R}^2$, in order to compensate for the decrease of the densities as the molecular wave packet spreads outward. The molecular axis $\boldsymbol{R}$ is defined as the position vector of the D atom relative to that of the Li atom. As shown in the right panel of Fig. 2(a), at time $t = 0$ fs the LiD molecules are oriented so that the molecular axes $\boldsymbol{R}$ of the LiD molecules point predominantly toward the positive z direction; the corresponding molecular wave packet is localized about the equilibrium bond length 3 a.u. Then the wave packet moves outward, spreading as it moves in the excited molecular potential. The wave packet reaches the outer turning point $R \approx 8$ a.u. at about $t = 58.0$ fs, after which the molecule oscillates backward in the second half of the vibration. Owing to the much longer time scale of the rotational motion, no appreciable change of the angular distribution is observed during the first few cycles of vibration.

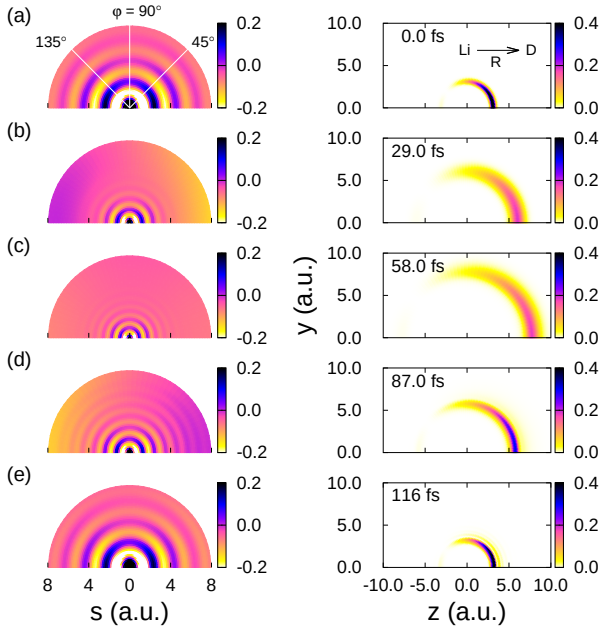

FIG. 2. *Right column*: Molecular density of the ro-vibrational motion of deuterated lithium hydride (LiD) in the excited state $A^1\Sigma^+$ as a function of time. The molecules are oriented at time $t = 0$ predominantly with the D atoms to the right of the Li atoms. The molecular density is weighted by the square of the internuclear distance, $\boldsymbol{R}^2$, in order to compensate for the decrease of the density as the atoms move apart. *Left column*: Time-resolved molecular scattering intensities of 1-fs (FWHM) 10 keV electron pulses from LiD molecules undergoing ro-vibrational motion; results are plotted as functions of the momentum transfer s and the azimuthal scattering angle φ at pump-probe delay times corresponding to those for the molecular densities in the right column. The color bars are in arbitrary units. Owing to symmetry, only the upper diffraction images and molecular densities are shown.

The time-resolved diffraction images for 1-fs (FWHM) electron pulses from LiD molecules undergoing ro-vibrational motion are shown in the left column of Fig. 2 as a function of the magnitude of the momentum transfer, s, and the azimuthal scattering angle φ. The magnitude of the momentum transfer is calculated using Eq. (11), since (for our high-energy incident electrons) inelastic transitions will not change the value of s significantly. At zero pump-probe delay [Fig. 2(a)], the diffraction image shows a concentric ring pattern, as in a Young's double slit experiment, resulting from interference of the scattering amplitudes from the Li and D atoms. The diffraction pattern is centrosymmetric and peaks in the $\varphi = 0°$ and 180° directions, reflecting the orientation of the molecules. (The peaking is most prominent for the inner rings.) As the bond length increases [Fig. 2(b)], the rings concentrate toward the forward direction $s = 0$ a.u. Meanwhile, the outer rings lose their visibility (*i.e.*, contrast). In addition to the usual ring pattern, the diffrac-

tion image at large momentum transfer ($s \gtrsim 4$ a.u.) exhibits an asymmetric angular distribution with respect to $\varphi = 90°$. The probability for the incident electrons to scatter toward the left ($\varphi = 180°$) is slightly larger than for scattering toward the right ($\varphi = 0°$). Furthermore, the asymmetry reverses its sign as the molecule oscillates backward [Fig. 2(d)]. Note that when the wave packet reaches the turning points [Figs. 2(a), (c), and (e)], the diffraction patterns are essentially centrosymmetric.

In order to better quantify the VOC effect in time-resolved UED, we define the *asymmetry* as the ratio of the difference between the values of the EASP $\langle \mathscr{P}(\varphi) \rangle$ [see Eqs. (8) and (9)] at $\varphi = 0°$ and 180° divided by their sum:

$$\text{Asymmetry} \equiv \frac{\langle \mathscr{P}(\varphi = 0°) \rangle - \langle \mathscr{P}(\varphi = 180°) \rangle}{\langle \mathscr{P}(\varphi = 0°) \rangle + \langle \mathscr{P}(\varphi = 180°) \rangle} . \quad (12)$$

The asymmetries at different time delays within the first half of a vibrational period are plotted as a function of momentum transfer in Fig. 3(a). At zero delay, the asymmetry is zero for all values of momentum transfer. When the molecule starts to vibrate, the asymmetry oscillates about zero for small momentum transfers ($s \lesssim 3$ a.u.) and then decreases monotonically for large values of s. The magnitude of the asymmetry for $s \gtrsim 3$ a.u. increases continuously until 29.0 fs, which roughly corresponds to the time at which the molecule is halfway toward the outer turning point of the vibrational motion. Thenceforth the magnitude decreases. In general, the magnitude of the asymmetry is largest at large momentum transfers for all time delays.

The EASP asymmetries for ultrafast x-ray scattering from the LiD molecule undergoing the same rovibrational motion are shown in Fig. 3(b). The x-ray results, taken from Ref. [47], are for an x-ray pulse whose central frequency is 59.3 keV and whose FWHM duration is 1.0 fs. The main difference between the electron and x-ray simulations is that the atomic scattering amplitude in UED includes additional contributions from the nuclei [*i.e.*, the Z_j term in Eq. (10)]. Comparing Figs. 3(a) and 3(b), one sees that the asymmetries in the case of x-rays have greater magnitudes and simpler behaviors (i.e., there are no oscillations about zero for small s). Nevertheless, the overall behaviors are still very similar, *i.e.*, for $s \gtrsim 3$ a.u. the asymmetries decrease essentially monotonically with increasing s and the maximum magnitudes occur for a time delay of 29.0 fs. In order to investigate the source of the sign oscillation for $s \lesssim 3$ a.u. in Fig. 3(a), we calculate the part of the asymmetry in UED originating from the nuclei, Li and D, by setting the atomic form factors $f_j(s)$ in Eq. (10) equal to zero. The results in Fig. 3(c) show that the sign oscillations disappear. Given that the x-ray asymmetries in Fig. 3(b) (in which the x-rays only scatter from the LiD electrons) also do not have oscillations for small values of s, the results in Fig. 3(c) suggest that the oscillations seen in Fig. 3(a) stem from interference of the UED scattering amplitudes from electrons and nuclei.

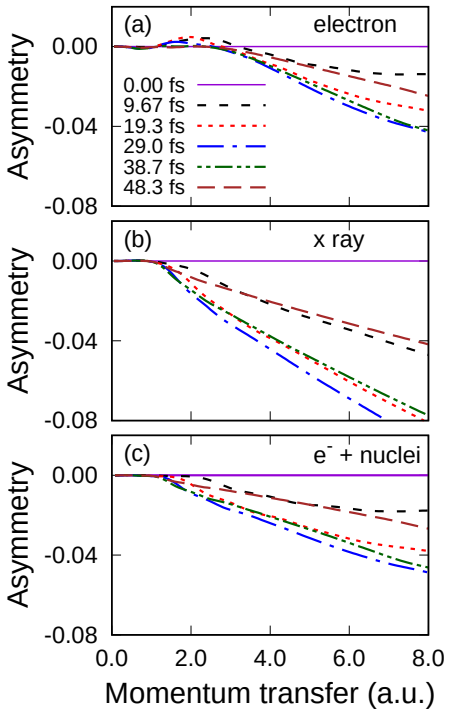

FIG. 3. Comparison of the EASP asymmetries, defined in Eq. (12), for (a) 1-fs ultrafast electron pulses and (b) 1-fs x-ray pulses scattered from LiD molecules undergoing rovibrational motion. The asymmetries are plotted as a function of momentum transfer s. Note that a negative asymmetry means that more incident electrons or x-ray photons are scattered toward $\varphi = 180°$ than toward $\varphi = 0°$. Different lines correspond to different pump-probe delay times as specified in the legend in panel (a). In panel (c), the asymmetry is calculated for scattering from the Li and D atomic nuclei alone, treated as point charges (i.e., neglecting scattering from the atomic electrons).

The contributions of UED from the LiD nuclei also have nontrivial effects on the molecular scattering intensities. Figure 4 compares the molecular scattering intensities, calculated as described in Sec. II E, for both 1-fs electron pulses [in Fig. 4(a)] and 1-fs x-ray pulses [in Fig. 4(b)] as a function of momentum transfer for six time delays in the first half period of the LiD vibrational motion. In all cases, the azimuthal angle is $\varphi = 0°$. Compared with the electron molecular scattering intensities, those for the x-rays quickly lose their contrast as the momentum transfer increases. One barely discerns any oscillatory behaviors beyond $s \approx 4$ a.u. for all delay times in Fig. 4(b), whereas such oscillations are clearly seen for the first three time delays in Fig. 4(a). The rapid decrease of the contrast even distorts the positions of the extreme in the x-ray case, thus affecting the determination of internuclear bond lengths. For example, the deepest minimum in the electron case (for a time delay $t = 0$ fs) occurs at $s \approx 1.4$ a.u., but this minimum is shifted to a slightly lower value ($s \approx 1.3$ a.u.) in the x-

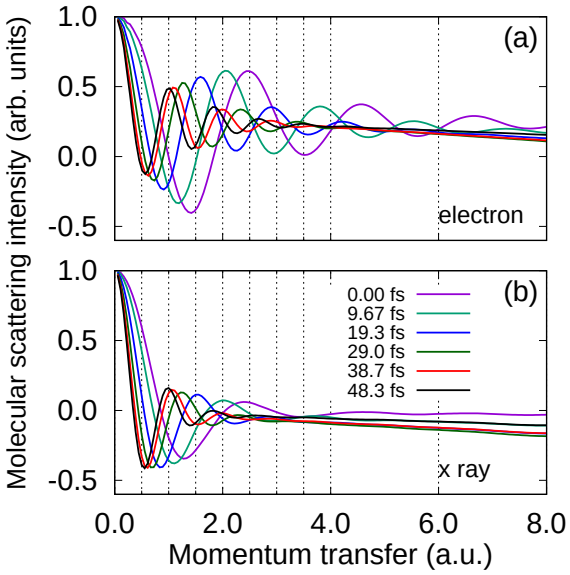

FIG. 4. Comparison of the molecular scattering intensities (calculated as described in Sec. II E) for (a) electron and (b) x-ray diffraction from the LiD molecule as a function of momentum transfer s for six different pump-probe delay times. In all cases, the azimuthal angle is $\varphi = 0°$. To facilitate comparisons, the molecular scattering intensities are normalized to the maximum intensity for time delay $t = 0$ fs and $s = 0$ a.u.

ray case.

B. Deuterated hydrogen molecule

Electron diffraction from a hydrogen molecule undergoing ro-vibrational motion does not exhibit any VOC in its diffraction images owing to the symmetry of the H_2 molecule. However, we show here that the VOC can occur in UED from the HD molecule undergoing ro-vibrational motion owing to the different velocities of the two isotopic atoms comprising the otherwise homonuclear diatomic molecule. We also show that there is a notable difference in the VOC effects exhibited in the UED images for scattering from the HD and LiD diatomic molecules.

Figure 5(a) shows the molecular potential energy curves of the ground $X^1\Sigma_g^+$ and excited $B^1\Sigma_u^+$ electronic states of the HD molecule, which are calculated using the complete active-space self-consistent field method from the Gaussian 16 package [65]. The excited potential curve is slightly shifted by 0.13 a.u. toward the origin to simplify the numerical computations. This shift changes the Franck-Condon factors, and, accordingly, the ensuing motion of the wave packet in the excited state. Without the shift the nuclei move faster and further from each other, and the wave packet spreads wider. Therefore, the spacing of the interference fringes and the degree of the VOC change as they reflect the internuclear distance and the nuclear motion, respectively. However, since the

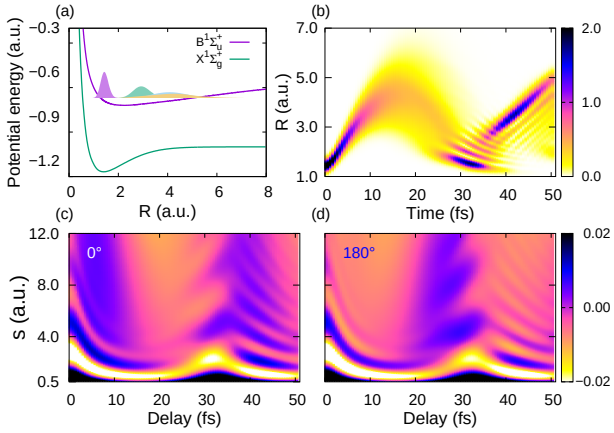

FIG. 5. (a) Molecular potential energy curves of the $X^1\Sigma_g^+$ and $B^1\Sigma_u^+$ states of the hydrogen molecule as a function of internuclear distance R. (b) The radial molecular wave packet for ro-vibrational motion of the deuterated hydrogen molecule (HD) in the excited $B^1\Sigma_u^+$ state as a function of time. The molecular scattering intensities for 1-fs (FWHM) 10 keV electron pulses from HD molecules undergoing ro-vibrational motion are shown for two azimuthal scattering angles: (c) $\varphi = 0°$ and (d) $\varphi = 180°$ [see Fig. 1(a) for definition of φ].

shift is small and the alteration of the nuclear motion seems insignificant, we think that the VOC-related features focused in the paper should remain the same. The radial molecular density in the $B^1\Sigma_u^+$ state as a function of time is plotted in Fig. 5(b). The molecular axis vector $\boldsymbol{R}$ points from the D atom to the H atom and, for the purpose of comparison, the orientation and angular distribution of the HD molecules at zero time delay are chosen to be the same as for the LiD molecules [see the right panel in Fig. 2(a)]. As seen in Fig. 5(b), the $B^1\Sigma_u^+$ state also supports a large vibration amplitude; however, the dispersion of the HD excited molecular wave packet is more significant than the dispersion shown in the right column of Fig. 2 for the LiD excited molecular wave packet.

The time-resolved molecular scattering intensities at $\varphi = 0°$ and $180°$ as a function of pump-probe delay are presented in Figs. 5(c) and 5(d), respectively. As for the LiD molecule, the interference fringes vary with the time delay, which reflects the vibrational motion of the HD molecule. In addition, comparing the results for $\varphi = 0°$ and $\varphi = 180°$, VOC can be observed at large momentum transfers $s \gtrsim 3.0$ a.u. as the molecule vibrates. Specifically, the scattering intensities at $\varphi = 0°$ are larger than those at $\varphi = 180°$ as the bond length increases, and the asymmetry changes its sign after the molecule reaches its outer turning point at a time delay of $t \approx 15$ fs. One sees also that the interference fringes for time delays of $5 \leq t \leq 30$ fs are not visible for large momentum transfers. Contrary to the LiD molecule, the VOC in the HD case is exclusively caused by the motion of the hydrogen atoms because, in our model, the atomic scattering amplitudes from the H and D atoms are identical. Notably, the asymmetries have opposite signs for the LiD and HD

molecules despite the fact that in both the LiD and HD cases the molecular axis $\boldsymbol{R}$ points from the heavy atom to the light one. Moreover, both molecules share the same initial orientation and angular distribution. However, whereas the scattering intensities increase in the direction of motion of the H atom in the HD case (*i.e.*, the direction of $d\boldsymbol{R}/dt$ or $\varphi = 0°$), they instead increase in the direction of motion of the Li atom in the LiD case (*i.e.*, the direction of $-d\boldsymbol{R}/dt$ or $\varphi = 180°$), as may be seen in the left column of Fig. 2.

IV. SEMI-CLASSICAL INTERPRETATION

Having seen the character of the time-resolved diffraction images from the molecular ro-vibrational motion, in this section we provide a semi-classical interpretation of the VOC in the diffraction images in Figs. 2 and 5 and discuss some implications from such interpretation. Since our interpretation utilizes Newton diagrams which are seldom applied in UED, we first introduce the Newton diagram in the simplest scenario: a binary collision in Sec. IV A. Then the simple scenario is generalized to a scattering from a vibrating molecule in Sec. IV B, where one will see how the VOC relates to the nuclear motion. Next, we argue that the interference fringes cannot be obtained simply by appending a position-dependent phase to the scattering amplitude, which is frequently employed in time-independent UED theory. Instead, we discuss in Sec. IV C that the interference fringes appear when both the projectile and molecule are treated as wave packets in a time-resolved scattering. Finally, we also say a few words about time-resolved coherent x-ray diffraction from the same semi-classical perspective in Sec. IV D.

A. Newton diagram for a binary collision

Since the velocities and angular distributions of reactants and products in collisions are measured in laboratory reference frames (hereafter, lab frames for short), these kinematic and dynamic quantities are usually transformed to center-of-mass (cm) frames to remove the overall cm motion for analyses and interpretations. The *Newton diagram* is a graphical device that facilitates such coordinate transformations and visualizes the relationships of velocities and differential scattering cross sections in both reference frames. Figure 6(a) shows the Newton diagram for an elastic collision between two beams of projectiles and scatterers crossing perpendicularly. In the lab frame, the velocities of the projectile and scatterer are denoted, respectively, by $\boldsymbol{v}_0$ (vertical arrow) and $\boldsymbol{v}_1$ (horizontal arrow), and the corresponding quantities in the cm frame are labeled with a prime (*i.e.*, $\boldsymbol{v}'_0$ and $\boldsymbol{v}'_1$). Since the velocities of the two particles are always counter-propagating in the cm frame, the velocity $\boldsymbol{v}_c$ of the cm frame must lie on the straight line connecting the heads of $\boldsymbol{v}_0$ and $\boldsymbol{v}_1$. The precise position of $\boldsymbol{v}_c$ along this line can be simply determined by the mass ratio of the projectile and scatterer, for the total linear momentum must be zero in the cm frame (*i.e.*, $m_0|\boldsymbol{v}'_0| = m_1|\boldsymbol{v}'_1|$, where m_0 and m_1 are the masses of the projectile and scatterer, respectively).

After the collision, the projectile recoils from the scatterer with an asymptotic velocity $\boldsymbol{v}_a$. For an elastic scattering, the conservation of energy and momentum dictates that, in the cm frame, only the trajectory of the projectile is deflected and there is no change of magnitude in its asymptotic velocity (*i.e.*, $|\boldsymbol{v}'_a| = |\boldsymbol{v}'_0|$). Accordingly, the velocities of all scattered projectiles lie on a circle centered at $\boldsymbol{v}_c$ with the radius $|\boldsymbol{v}'_0|$ [which is the blue circle in Fig. 6(a)]. The angular distribution of the scattered projectiles on this *Newton circle* depends on the dynamics of the collision (*i.e.*, the scattering mechanism). From the Newton diagram one sees that, in the cm frame, the projectile moves in the direction of 11 o'clock and the "physical" scattering angle $\theta' \equiv \angle(\boldsymbol{v}'_0, \boldsymbol{v}'_a)$ should be measured with respect to $\boldsymbol{v}'_0$, while in the lab frame the scattering angle $\theta \equiv \angle(\boldsymbol{v}_0, \boldsymbol{v}_a)$ is defined with respect to $\boldsymbol{v}_0$. Moreover, the kinetic energy of the scattered projectile can differ from the incident one in the lab frame [*e.g.*, $|\boldsymbol{v}_a| > |\boldsymbol{v}_0|$ in Fig. 6(a)], even though the scattering is elastic.

As a consequence of the transformation between the lab and cm frames, differential cross sections (DCSs) of the projectile in the two frames are related by the Jacobian of the coordinate transformation. The DCS transforms as [66–68]

$$\frac{d\sigma}{d\Omega} = \frac{d\sigma}{d\Omega'}\left|\frac{d\Omega'}{d\Omega}\right| = \frac{d\sigma}{d\Omega'}\frac{\boldsymbol{v}_a^2}{\boldsymbol{v}_a'^2}\left|\cos\delta\right|, \tag{13}$$

where $d\sigma/d\Omega$ and $d\sigma/d\Omega'$ are the respective DCSs in the lab and cm frames, and $\delta \equiv \angle(\boldsymbol{v}_a, \boldsymbol{v}'_a)$ is the angle between $\boldsymbol{v}_a$ and $\boldsymbol{v}'_a$. Geometrically, the ratio of the velocity square in Eq. (13) is responsible for the change of areas of the surface elements (subtended by the solid angles $d\Omega$ and $d\Omega'$ in the lab and cm frames, respectively) in the transformation, and $\cos\delta$ takes account of the projection of the flux normal to the surface element. Because of the Jacobian factor, as long as the velocity $\boldsymbol{v}_c$ of the cm frame has a nonzero transverse component with respect to the velocity $\boldsymbol{v}_0$ of the incident projectile, the DCS in the lab frame exhibits an asymmetric angular distribution with respect to the forward direction $\theta = 0°$, even though the angular distribution $d\sigma/d\Omega'$ in the cm frame is symmetric with respect to $\theta' = 0°$. Figure 6(b) depicts an example of the DCS in the lab frame for the collision geometry in Fig. 6(a) with an assumption that the DCS is isotropic in the cm frame. Namely, it shows the Jacobian of the transformation as functions of scattering angles θ and φ. One can clearly see the projectiles are more probable to scatter toward right direction (*i.e.*, $\varphi < 90°$), and this asymmetry in the DCS reflects the (trivial) cm motion in the binary collision.

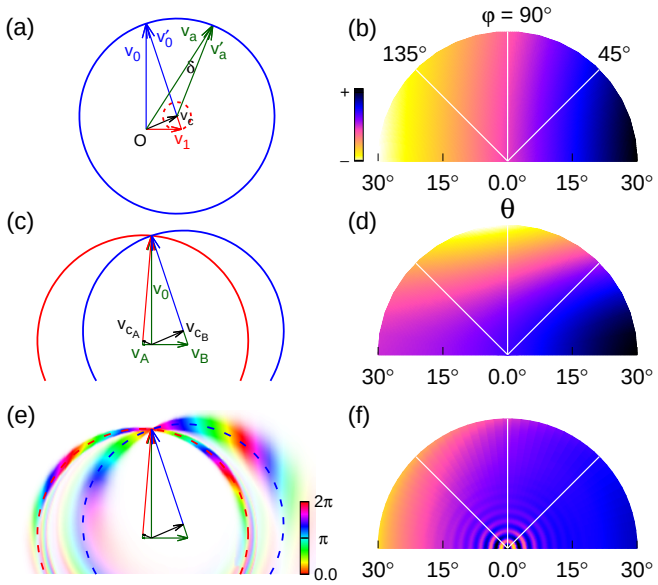

FIG. 6. Semi-classical interpretation of the asymmetry and interference fringes in coherent diffraction from ro-vibrational motion of diatomic molecules. (a) Newton diagram for a binary collision of two beams of projectiles and scatterers. The origin of the diagram is labeled by O. The velocities of the incident projectile and scatter are denoted, respectively, by $\boldsymbol{v}_0$ and $\boldsymbol{v}_1$, and the velocity of the scattered projectile is denoted by $\boldsymbol{v}_a$. The velocity of the center-of-mass (cm) frame is $\boldsymbol{v}_c$, and the velocities with respect to the cm frame are labeled with a prime (*e.g.*, $\boldsymbol{v}'_a$). The circles with solid and dash lines are the Newton circles for the elastically scattered projectiles and scatterers, respectively. The parameters are $m_1/m_0 = 7$ and $|\boldsymbol{v}_1|/|\boldsymbol{v}_0| = 1/3$. (b) Asymmetric differential cross section (DCS) of the projectile in the lab frame resulting from the cm motion. The DCS is generated using Eq. (13) by assuming that the DCS in the cm frame is isotropic. (c) Newton diagram for the scattering of projectiles from heteronuclear diatomic molecules AB. At the moment of collision, the molecule is vibrating such that the velocities of the atoms A and B are $\boldsymbol{v}_A$ and $\boldsymbol{v}_B$, respectively. The parameters are $m_A/m_0 = 28$, $m_B/m_0 = 7$, $|\boldsymbol{v}_A|/|\boldsymbol{v}_0| = 1/12$, and $|\boldsymbol{v}_B|/|\boldsymbol{v}_0| = 1/3$. (d) VOC in the DCS of the projectile scattered from the vibrating AB molecule. The DCSs of both A and B are isotropic in their own cm frames but with different scattering intensities: $\sigma'_A/\sigma'_B = 4$. (e) Newton diagram for pulsed projectiles scattered from a vibrating *molecular wave packet* of AB. The color and its shade of brightness indicate the phase and magnitude of the scattering amplitudes $\mathscr{A}(\boldsymbol{v}_a)$ [see Eq. (15)], respectively. The velocity distributions of the atoms are assumed to be two-dimensional Gaussian distributions with widths $\delta\boldsymbol{v}_j$, and the velocity distribution of the projectile has a one-dimensional Gaussian envelope with a width $\delta\boldsymbol{v}_{0y}$. The parameters are $\delta\boldsymbol{v}_{0y}/|\boldsymbol{v}_0| = 1/150$, and $|\delta\boldsymbol{v}_j|/|\boldsymbol{v}_j| = 1/2$ ($j = A$, B). (f) Example of a time-resolved diffraction image from the vibrating molecular wave packet.

B. Newton diagram for a collision from a vibrating molecule

Now let us replace the scatterers by some (fictitious) diatomic molecules AB whose cm is at rest in the lab frame. Assume that, at the moment of collision, the molecule is vibrating such that the velocities of atoms A and B are $\boldsymbol{v}_A$ and $\boldsymbol{v}_B$, respectively, as shown in Fig. 6(c). If one neglects the influence of the other atom when the projectile collides with one of the atoms, then the scattering can be considered as a sum of two independent scatterings from the atoms A and B (*i.e.*, independent-atom model). Accordingly, the DCS of the projectile-molecule scattering is a sum of the DCSs of the constituent atoms. As indicated in Fig. 6(c), the DCSs of atoms A and B exhibit opposite asymmetries, for the horizontal components of their cm velocities point in opposite directions, and the overall asymmetry of the total DCS is a result of the competition between the asymmetries of A and B. In Fig. 6(d), we show the DCS of the projectile scattered from the vibrating AB molecule, assuming that the DCSs of A and B are isotropic in their own cm frames but the scattering intensity of A is four times stronger than that of B. The DCS manifests VOC asymmetry, but the degree of the asymmetry is reduced as compared with Fig. 6(b). In short, from the perspective of the Newton diagrams in Figs. 6(a) and (c), the VOC effect in diffraction images is a direct consequence of scattering kinematics of reference frame transformation as one measures the scattering intensities from moving particles.

Three corollaries can be inferred from the above observations of the Newton diagram in Fig. 6(c). First, anisotropy of *molecular geometry* alone is insufficient to break the centrosymmetry of diffraction patterns; however, disparity between *particles' motion* is necessary to produce the asymmetry. As shown in the right column of Fig. 2, the heteronuclear LiD molecules maintain their orientation (*i.e.*, geometric anisotropy) throughout the first few cycles of the vibrational motion, and the diffraction images can still exhibit centrosymmetry as seen in

Figs. 2(a), (c), and (e). However, VOC occurs as the oriented molecules start vibrating [Fig. 2(b)], and the asymmetry reverses its sign as the Li and D atoms flip their directions of motion after reaching the outer turning point [Fig. 2(d)]. Furthermore, anisotropy in molecular motion solely is enough to break the centrosymmetry. For the case of homonuclear HD molecules, orientation is irrelevant to geometric anisotropy because in our model, from the perspective of the incident electrons, the H and D atoms are electronically identical when they are stationary, but the VOC can still be seen resulting from the rovibrational motion in Figs. 5(c) and (d). In addition, this asymmetry exists in any reference frame because it reflects the relative motion of the constituent atoms rather than the overall cm motion of the molecule.

Second, the degree of VOC asymmetry pertains to the velocity of a scatterer, not its momentum. Given that AB is at rest in the lab frame, the magnitudes of the momenta of A and B are the same (*i.e.*, $m_A|\boldsymbol{v}_A| = m_B|\boldsymbol{v}_B|$), but the lighter atom B has larger cm velocity $\boldsymbol{v}_{c_B}$, thus inducing a greater degree of asymmetry. Moreover, the competition of the asymmetry for a diatomic molecule depends on the relative velocities (or masses) and scattering intensities of the constituent atoms. However, these factors usually tend to counteract to each other. As the molecule vibrates, although the light atom moves faster, thus rendering a bigger asymmetry in its DCS, the heavier one usually has stronger scattering intensity, thus dominating the overall DCS. This is what we observed in the cases of LiD and HD molecules. In the HD case, both H and D atoms have the same atomic scattering amplitude in our model, but since the H atom moves faster in the vibrational motion, the asymmetry reflects the motion of the H atom (*i.e.*, the scattering intensity increases in the same direction of motion of the H atom). On the other hand, in the LiD case, although the D atom moves faster, the Li atom has larger scattering intensity. As a result, the asymmetry indicates the motion of the Li atom.

Third, the momentum transfer $\boldsymbol{s} = m_0\,(\boldsymbol{v}_0 - \boldsymbol{v}_a)$ calculated without considering the cm motion (thus, $|\boldsymbol{v}_a| \stackrel{!}{=} |\boldsymbol{v}_0|$ for elastic scattering) is only approximate, though in typical situations of UED such approximation can be quite accurate (see caution in the last paragraph of Sec. IV C).

While the above classical picture renders an intuitive interpretation of the asymmetry in time-resolved diffraction images, an important feature of coherent diffraction, namely the interference fringe, is absent from the DCS in Fig. 6(d). Microscopic particles also exhibit wave behaviors, possessing probability amplitudes and phases. Hence, treated as a matter wave, a scattered projectile carries a scattering amplitude $f(\boldsymbol{s})$ with a phase $e^{i\boldsymbol{s}\cdot\boldsymbol{R}_j}$ depending on the position $\boldsymbol{R}_j$ of the scatterer. Under the independent-atom model, the total scattering amplitude

$$f(\boldsymbol{s}) = f_A(s)\,e^{i\boldsymbol{s}\cdot\boldsymbol{R}_A} + f_B(s)\,e^{i\boldsymbol{s}\cdot\boldsymbol{R}_B} \tag{14}$$

is a sum of the scattering amplitudes from A and B, and the DCS is the absolute square of the scattering amplitude, $d\sigma/d\Omega = |f(\boldsymbol{s})|^2$ (strictly speaking, for elastic scattering). Therefore, interference fringes arise as the two amplitudes in Eq. (14) interfere, yielding a modulation in the DCS that oscillates as a function of momentum transfer $\boldsymbol{s}$.

However, even by assigning the position-dependent phases $e^{i\boldsymbol{s}\cdot\boldsymbol{R}_A}$ and $e^{i\boldsymbol{s}\cdot\boldsymbol{R}_B}$ to the Newton circles of A and B, respectively, in Fig. 6(c), no interference fringes can emerge because the two Newton circles intersect (at most) at two points. In other words, the projectiles recoil from the atoms A and B with different speeds in almost every direction (even though each scattering event is elastic). These scattered projectiles correspond to states with different asymptotic momenta and, therefore, their scattering amplitudes do not interfere (in conventional DCS measurements). This is still true even there is no vibration (*i.e.*, both A and B are at rest in the lab frame). This counterintuitive circumstance lies in the fact that the Newton diagram in Fig. 6(c), wave mechanically, does not represent a vibrating molecule. Molecules have well-defined geometries and their constituent atoms vibrate around their equilibrium positions. However, since the velocities of the atoms A and B are well defined (*i.e.*, no uncertainty in their momenta), the uncertainty in the positions of the atoms is actually infinite, according to the uncertainty relation.

C. Newton diagram for a collision from a molecular wave packet

To rectify this, the molecule should be modeled as a wave packet with some distribution associated with the molecular geometry and motion. Figure 6(e) illustrates this by modeling the atoms A and B as wave packets with Gaussian amplitudes in velocity. The incident projectile is also considered as a wave packet for the time-dependent collision, having a Gaussian distribution along the vertical direction with a width δv_{0y}. Then the scattering amplitude $\mathscr{A}$ from the wave packet of atom j, where $j = A$ or B, is obtained by convoluting the scattering amplitude $f_j(s)$ with the probability amplitudes of the projectile $a_0(\boldsymbol{v}_{0y})$ and the atom $a_j(\boldsymbol{v}_j)$ under the constraints of elastic scattering:

$$\mathscr{A}(\boldsymbol{v}_a) \propto \int d\boldsymbol{v}_{0y}\,d\boldsymbol{v}_j\,a_0(\boldsymbol{v}_{0y})\,a_j(\boldsymbol{v}_j)\,f_j(s)\,e^{i\boldsymbol{s}\cdot\boldsymbol{R}_j}\,. \tag{15}$$

The scattering amplitude $f_j(s)$ is assumed to be symmetric with respect to the physical forward direction $\theta' = 0^\circ$ and decreases as $\propto 1/s$. For the position-dependent phase $e^{i\boldsymbol{s}\cdot\boldsymbol{R}_j}$, the molecule is further assumed to be aligned along the direction of vibration (*i.e.*, the direction of velocity $\boldsymbol{v}_j$) with a fixed length R_j. (Note that this deviates from a pure quantal treatment in that both the momentum and position distributions of the atoms A and B are specified.)

Owing to uncertainty in the velocities, the Newton circles in Fig. 6(c) become non-concentric shells as seen in

Fig. 6(e). Therefore, as the two *Newton shells* overlap, the scattering amplitudes from A and B can interfere. Figure 6(f) shows an example of the time-resolved diffraction image (which is taken from the LiD case). The interference fringes can be seen now but only in the small scattering angle ($\theta \lesssim 10^\circ$), and the fringe visibility fades as θ increases. On the other hand, the asymmetry is more prominent at large scattering angle ($\theta \gtrsim 15^\circ$) where the interference fringes disappear. This can be understood by examining the Newton diagram in Fig. 6(e). Due to the off-centered Newton shells, the two shells overlap less significantly at larger scattering angle than in the forward direction, thus the visibility of the interference fringes degrades. This anticorrelation between the fringe visibility and the degree of the asymmetry interestingly demonstrates the uncertainty relation of complementary variables of position and momentum because the interference fringes come from the relative positions of the atoms but the asymmetry is due to their motions. We note that the above explanation only partially accounts for the loss of the visibility which can also be attributed from the spreading (*i.e.*, delocalization) of the molecular wave packet.

Some remarks about the above semi-classical interpretation are in order. (i) The loss of fringe visibility and VOC effect in diffraction measurements are direct consequences of molecular motion. While reduced visibility may increase the uncertainty in determination of molecular geometry, it nevertheless reflects the nature of a molecular motion. However, we found that by reducing the pulse duration (*i.e.*, analogous to a faster shutter speed) to "freeze particles' motion" can enhance the visibility, though it is still unable to avoid the uncertainty resulting from the delocalization of molecular wave packet. (ii) While the interpretation is compatible with our quantum formulation [see the discussion of Eq. (10)], there are some physics unable to be (easily) captured by the simple picture using the independent-atom model. One aspect is the correlation between the motions of the constituent atoms in a molecule. Because of molecular bonding, atomic movements are not independent. Therefore, not all components in Newton shells lead to an interference when they overlap in a Newton diagram; two atomic scattering amplitudes can interfere only under certain conditions. For example, in Fig. 6(e) two amplitudes interfere, in addition to satisfying the conservation laws, when the velocities of A and B are such that the cm velocity of AB is at rest in the lab frame (*i.e.*, $m_A|\boldsymbol{v}_A| = m_B|\boldsymbol{v}_B|$). Another missed aspect is that no inelastic transitions between ro-vibrational states are included in the scattering amplitudes $\mathscr{A}(\boldsymbol{v}_a)$. On the other hand, the quantum simulations include all transitions among the ro-vibrational states [*i.e.*, the second line of Eq. (10)]. According to the discussion in Sec. II B, we know that such interference of the inelastic transitions plays nontrivial role in time-dependent scattering, imposing delay dependence and temporal resolution in time-resolved measurements. (iii) Coherent diffraction from *electronic motion* in atoms and molecules also exhibits the VOC effect [41, 43, 45, 48–50]. The physical mechanism behind this asymmetry should be the same as in the molecular motion; however, electronic motion exhibits more wave characteristic because, compared with nuclear states, electronic states are more delocalized in space and energy spacing is larger.

Before concluding the discussion of the semi-classical interpretation, we want to caution readers. In order to illustrate the physical mechanism behind the VOC effect in time-resolved diffraction, the parameters chosen to draw the Newton diagrams in Fig. 6 are exaggerated. In typical UED, the speeds $|\boldsymbol{v}_0|$ of incident electrons are usually orders of magnitude larger than the motions of constituent atoms in molecules, and the mass of electron is also orders of magnitude smaller than those of atoms. Therefore, the cm velocity of each electron-atom pair is very small, and, accordingly, the asymmetry is weak. In many cases, the cm frame can be approximated as stationary in the lab frame. This explains why we found that the VOC asymmetry is most significant in large amplitude vibrations of diatomic molecules involving hydrogen atom. In addition, the theory is based on the first-order Born approximation in non-resonant diffraction. Other mechanisms such as resonant and multiple scatterings may induce asymmetry as well. Similar VOC phenomenon has also been observed in photoionization spectra [69–71].

D. Semi-classical interpretation for x-ray diffraction

Although the nature of photons and their interaction with charged particles are very different from those of electrons, under the circumstances of non-resonant, first-order perturbative interaction the formulation describing time-dependent x-ray diffraction [47] is essentially equivalent to the UED one. Therefore, the same semi-classical picture should also be applied to the x-ray diffraction. In the theory of classical electrodynamics, the scattering of electromagnetic radiation from a (stationary or moving) charged particle can be considered as a process of re-emission of the radiation from the driven oscillatory motion of the particle. From the perspective of the rest frame of a moving electron, the scattering is simply the Thomson scattering (or the Compton scattering if the momentum of the photon is significant), so the DCS is centrosymmetric. However, from the perspective of the lab frame, the angular distribution of the re-emitted radiation shows asymmetric pattern resulting from the reference frame transformation. In order to apply the formulation used in UED, the analysis needs to be modified, as there is no cm frame for photon scattering. Instead of the center-of-mass frame, analogous analysis can be performed using the center-of-momentum frame in which the total momentum of the scattering system is zero. The coordinate transformation between the laboratory

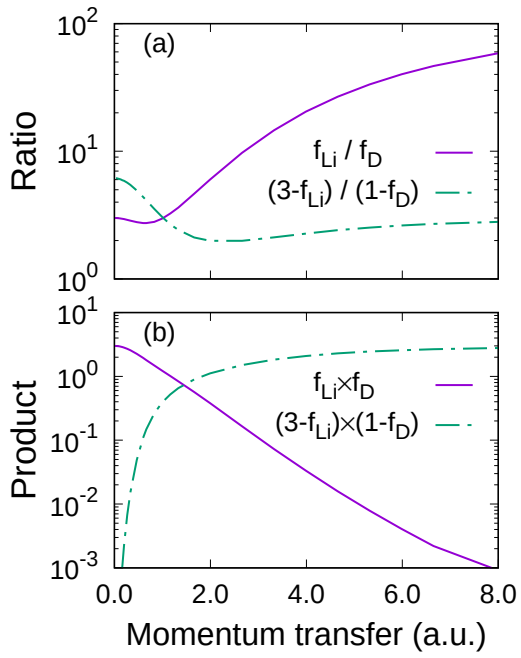

FIG. 7. (a) Ratio and (b) product of the atomic scattering amplitudes from Li and D atoms for x-ray (solid line) and electron (dash-dotted line) diffraction. In the x-ray case, the atomic scattering amplitude includes only the contribution from the electrons [*i.e.*, atomic form factor $f_j(s)$], but in the electron case, both the nucleus and electrons contribute to the scattering amplitude [see Eq. (10)].

and center-of-momentum frames is similar to the one in Eq. (13) in which variables like $\boldsymbol{v}_a$ are replaced by the corresponding ones like $\boldsymbol{k}_a$, provided that relativistic effect is negligible. Accordingly, many of the above UED corollaries are still applicable to the x-ray diffraction.

We would also like to explain the differences in the asymmetry (Fig. 3) and the molecular scattering intensity (Fig. 4) between the electron and x-ray diffraction from LiD molecules, applying the insights learned from the semi-classical picture. Since the molecular motions are identical in both cases, the differences come from the differences in the probe pulses and/or the scattering mechanisms. According to the previous paragraphs, the main characteristic of the probe pulse that affects the asymmetry (via the Jacobian factor) is its velocity/momentum distribution. However, we only found weak dependence of the asymmetry on the momentum of the incident particles. Thus, the main factor contributing to the differences results from the scattering mechanism, namely, the atomic scattering amplitude in Eq. (10). From Figs. 6(c) and (d), we know that the asymmetry is mainly contributed from the atomic scattering rather than from the molecular scattering (*i.e.*, the interference of atomic scattering amplitudes) and that the competition of the asymmetry depends on the relative strength of the scattering intensities from Li and H atoms. Therefore, in Fig. 7(a) we plot the ratios of the atomic scattering amplitude of Li atom to that of D atom for the x-ray (solid line) and electron (dash-dotted line) diffraction as a function of momentum transfer. In addition to the contribution from the atomic electrons, the scattering amplitude for the electron diffraction includes the contribution from the nucleus. One can see that for both cases the ratios are larger than one. The ratio for the electron diffraction has a maximum at zero momentum transfer, and the ratio falls and approaches to the ratio of the nucleus charge $Z_{\rm Li}/Z_{\rm D}$ as the momentum transfer increases. In contrast, except for small momentum transfer, the ratio for the x-ray case is larger than that of the electron and monotonically increases with the momentum transfer. Since the scattering from the Li atom dominates the scattering intensities (thereby the asymmetry), the ratios explain why the asymmetry of the x-ray case is stronger than that of the electron case.

Figure 4 shows that the molecular scattering intensities of UED have more prominent interference fringes at large momentum transfer than those of x-ray diffraction. Unlike the asymmetry, the modulation of the scattering intensities comes from the molecular scattering, so we plot the product of the atomic scattering amplitudes for the x-ray and electron cases in Fig. 7(b). We see opposite behaviors in the two cases. The product for the x-ray diffraction monotonically decreases, but the product for the electron case increases monotonically and approaches to the constant $Z_{\rm Li} \times Z_{\rm D}$. This explains why the visibility decreases so fast for the x-ray diffraction.

V. SUMMARY AND DISCUSSION

We have discussed the basic ideas of modeling time-dependent UED and presented the time-resolved UED imaging of ro-vibrational motion of diatomic molecules LiD and HD. The simulated diffraction images show delay-dependent interfering ring patterns that reflect the molecular orientation and the change of the internuclear distance during the vibrational motion. In addition, the diffraction images exhibit asymmetric angular distributions whenever the vibrational motion of the two atoms breaks the inversion symmetry. The comparison of the electron and x-ray diffraction in the case of LiD molecule shows that the presence of the scattering from the nuclei indeed affects the asymmetry and molecular scattering intensities in UED. The scattering from the nuclei enhances the contrast of the ring patterns at large scattering angle θ but slightly reduces the degree of the asymmetry.

We also present a semi-classical interpretation for the origin of the VOC asymmetry, the change of the sign of the asymmetry from the LiD to HD molecules, and the anticorrelation between the visibility of the interference fringes and the degree of the VOC. These phenomena can be understood as consequences of the scattering kinematics of reference frame transformation. In a UED from a moving scatterer, a symmetric DCS in the cm

frame can appear asymmetric in the lab frame because of the reference frame transformation [see Eq. (13)]. The sign and degree of the asymmetry respectively indicate the direction and magnitude of the scatterer's velocity with respect to the incident electron. Moreover, electrons scattered from the different atoms of a vibrating diatomic molecule render opposite asymmetries because of the countermovement of the atoms. The competition of the asymmetries results in the sign change of the overall asymmetry between the LiD and HD molecules. Likewise, since the velocity of a scattered electron depends on the motion of the scatterer at the moment of scattering, electrons scattered toward the same direction but from different atoms can recoil with different speeds if the molecule is vibrating. Thus, their scattering amplitudes may not interfere, and the contrast of the interference fringes degrade accordingly. The degradation is most significant when there occurs the highest disparity between the atoms' motion. With the help of Newton diagrams, the scattering kinematics of reference frame transformation can be easily visualized, and the above phenomena can be intuitively understood.

Finally, we remark the feasibility of creating an anisotropic nuclear motion. Our scheme in Sec. I involves a pre-oriented diatomic molecule before the pump process so that the excited wave packet exhibits an anisotropic nuclear vibration. A number of techniques have been developed or proposed to orient molecules using a static electric field, laser pulses, few-cycle terahertz pulses, or a combination of them [72–75]. Orientation of a molecule is typically separated into two regimes: adiabatic and nonadiabatic, based on the relative time scale between the pulse duration and the rotational period of the molecule. A long-term, high-degree orientation can usually be achieved in the adiabatic regime where molecular rotational states with different J, following an external strong field adiabatically, evolve to pendular states that liberate about the orientation axis. However, the presence of the external field can influence the motion of the incident electron pulses. On the other hand, a field-free orientation can be achieved in the nonadiabatic regime where a short pulse produces a coherent rotational wave packet that orients transiently after the pulse is gone. In particular, for lithium hydride, simulations have been shown high-degree orientations are possible using few-cycle terahertz pulses [59–61].

Instead of pre-orientation, it is possible, but with a caveat, to create a vibrational wave packet and orient a molecule simultaneously with a single pulse. Since a very different time scale between a rotational and a vibrational motion, the vibrational motion may have been dephased (*i.e.*, the vibrational wave packet has been delocalized) as the rotational wave packet orients.

ACKNOWLEDGMENTS

This work was supported in part by the U.S. National Science Foundation under Grant No. PHY-1505492. This work was completed utilizing the Holland Computing Center of the University of Nebraska, which receives support from the Nebraska Research Initiative.

[1] A.H. Zewail, 4D Ultrafast Electron Diffraction, Crystallography, and Microscopy, Annu. Rev. Phys. Chem. **57**, 65 (2006).
[2] R.J.D. Miller, Ultrafast imaging of photochemical dynamics: roadmap to a new conceptual basis for chemistry, Faraday Discuss. **194**, 777 (2016).
[3] M. Chergui and A.H. Zewail, Electron and X-ray Methods of Ultrafast Structural Dynamics: Advances and Applications, Chem. Phys. Chem. **10**, 28 (2009).
[4] T. Elsaesser and M. Woerner, Perspective: Structural dynamics in condensed matter mapped by femtosecond x-ray diffraction, J. Chem. Phys. **140**, 020901 (2014).
[5] R.J.D. Miller, Femtosecond Crystallography with Ultrabright Electrons and X-rays: Capturing Chemistry in Action, Science **343**, 1108 (2014).
[6] C. Bostedt, S. Boutet, D.M. Fritz, Z. Huang, H.J. Lee, H.T. Lemke, A. Robert, W.F. Schlotter, J.J. Turner, and G.J. Williams, Linac Coherent Light Source: The first five years, Rev. Mod. Phys. **88**, 015007 (2016).
[7] D.J. Flannigan and A.M. Lindenberg, Atomic-scale imaging of ultrafast materials dynamics, MRS Bulletin **43**, 485 (2018).
[8] G. Sciaini and R.J.D. Miller, Femtosecond electron diffraction: heralding the era of atomically resolved dynamics, Rep. Prog. Phys. **74**, 096101 (2011).
[9] M. Centurion, Ultrafast imaging of isolated molecules with electron diffraction, J. Phys. B: At. Mol. Opt. Phys. **49**, 062002 (2016).
[10] P. Baum and F. Krausz, Capturing atomic-scale carrier dynamics with electrons, Chem. Phys. Lett. **683**, 57 (2017).
[11] J.M. Thomas, R.K. Leary, A.S. Eggeman, and P.A. Midgley, The rapidly changing face of electron microscopy, Chem. Phys. Lett. **631-632**, 103 (2015).
[12] A. Adhikari, J.K. Eliason, J. Sun, R. Bose, D.J. Flannigan, and O.F. Mohammed, Four-Dimensional Ultrafast Electron Microscopy: Insights into an Emerging Technique, ACS Appl. Mater. Interfaces **9**, 3 (2017).
[13] M.Th. Hassan, Attomicroscopy: from femtosecond to attosecond electron microscopy, J. Phys. B **51**, 032005 (2018).
[14] X. Shen, R.K. Li, U. Lundström, T.J. Lane, A.H. Reid, S.P. Weathersby, and X.J. Wang, Femtosecond mega-electron-volt electron microdiffraction, Ultramicroscopy **184**, 172 (2018).
[15] J. Breuer and P. Hommelhoff, Laser-Based Acceleration of Nonrelativistic Electrons at a Dielectric Structure, Phys. Rev. Lett. **111**, 134803 (2013).
[16] E.A. Peralta *et al.*, Demonstration of electron acceleration in a laser-driven dielectric microstructure, Nature (London) **503**, 91 (2013).

[17] R.J. England *et al.*, Dielectric laser accelerators, Rev. Mod. Phys. **86**, 1337 (2014).

[18] J. McNeur *et al.*, Elements of a dielectric laser accelerator, Optica **5**, 687 (2018).

[19] D.S. Black, K.J. Leedle, Y. Miao, U. Niedermayer, R.L. Byer, and O. Solgaard, Laser-Driven Electron Lensing in Silicon Microstructures, Phys. Rev. Lett. **122**, 104801 (2019).

[20] A. Gliserin, A. Apolonski, F. Krausz, and P. Baum, Compression of single-electron pulses with a microwave cavity, New J. Phys. **14**, 073055 (2012).

[21] P. Zhu *et al.*, Femtosecond time-resolved MeV electron diffraction, New J. Phys. **17**, 063004 (2015).

[22] S.P. Weathersby *et al.*, Mega-electron-volt ultrafast electron diffraction at SLAC National Accelerator Laboratory, Rev. Sci. Instrum. **86**, 073702 (2015).

[23] J. Maxson, D. Cesar, G. Calmasini, A. Ody, P. Musumeci, and D. Alesini, Direct Measurement of Sub-10 fs Relativistic Electron Beams with Ultralow Emittance, Phys. Rev. Lett. **118**, 154802 (2017).

[24] O. Zandi, K.J. Wilkin, Y. Xiong, and M. Centurion, High current table-top setup for femtosecond gas electron diffraction, Struct. Dyn. **4**, 044022 (2017).

[25] E.A. Nanni, W.R. Huang, K.-H. Hong, K. Ravi, A. Fallahi, G. Moriena, R.J.D. Miller, and F.X. Kärtner, Terahertz-driven linear electron acceleration, Nat. Commun. **6**, 8486 (2015).

[26] C. Kealhofer, W. Schneider, D. Ehberger, A. Ryabov, F. Krausz, and P. Baum, All-optical control and metrology of electron pulses, Science **352**, 429 (2016).

[27] D. Zhang *et al.*, Segmented terahertz electron accelerator and manipulator (STEAM), Nat. Photon. **12**, 336 (2018).

[28] D. Ehberger, K.J. Mohler, T. Vasileiadis, R. Ernstorfer, L. Waldecker, and P. Baum, Terahertz Compression of Electron Pulses at a Planar Mirror Membrane, Phys. Rev. Applied **11**, 024034 (2019).

[29] M.T. Hassan, H. Liu, J.S. Baskin, and A.H. Zewail, Photon gating in four-dimensional ultrafast electron microscopy, Proc. Natl. Acad. Sci. USA **112**, 12944 (2015).

[30] M.Th. Hassan, J.S. Baskin, B. Liao, and A.H. Zewail, High-temporal-resolution electron microscopy for imaging ultrafast electron dynamics, Nat. Photon. **11**, 425 (2017).

[31] J. Yang *et al.*, Imaging CF_3I conical intersection and photodissociation dynamics with ultrafast electron diffraction, Science **361**, 64 (2018).

[32] T.J.A. Wolf *et al.*, The photochemical ring-opening of 1,3-cyclohexadiene imaged by ultrafast electron diffraction, Nat. Chem. **11**, 504 (2019).

[33] V.R. Morrison, R.P. Chatelain, K.L. Tiwari, A. Hendaoui, A. Bruhács, M. Chaker, and B.J. Siwick, A photoinduced metal-like phase of monoclinic VO_2 revealed by ultrafast electron diffraction, Science **346**, 445 (2014).

[34] L. Waldecker, T.A. Miller, M. Rudé, R. Bertoni, J. Osmond, V. Pruneri, R.E. Simpson, R. Ernstorfer, and S. Wall, Time-domain separation of optical properties from structural transitions in resonantly bonded materials, Nature Mater. **14**, 991 (2015).

[35] T. Ishikawa *et al.*, Direct observation of collective modes coupled to molecular orbital-driven charge transfer, Science **350**, 1501 (2015).

[36] L. Wei *et al.*, Dynamics diffraction effects and coherent breathing oscillations in ultrafast electron diffraction in layered 1*T*-TaSeTe, Struct. Dyn. **4**, 044012 (2017).

[37] T. Frigge *et al.*, Optically excited structural transition in atomic wires on surfaces at the quantum limit, Nature **544**, 207 (2017).

[38] M.J. Stern, L.P. René de Cotret, M.R. Otto, R.P. Chatelain, J.-P. Boisvert, M. Sutton, and B.J. Siwick, Mapping momentum-dependent electron-phonon coupling and nonequilibrium phonon dynamics with ultrafast electron diffuse scattering, Phys. Rev. B **97**, 165416 (2018).

[39] M.Z. Mo *et al.*, Heterogeneous to homogeneous melting transition visualized with ultrafast electron diffraction, Science **360**, 1451 (2018).

[40] A. Feist, G. Storeck, S. Schäfer, and C. Ropers, Structural dynamics probed by high-coherence electron pulses, MRS Bulletin **43**, 504 (2018).

[41] H.-C. Shao and A.F. Starace, Imaging coherent electronic motion in atoms by ultrafast electron diffraction, Phys. Rev. A **88**, 062711 (2013).

[42] H.-C. Shao and A.F. Starace, Imaging electronic motions in atoms by energy-resolved ultrafast electron diffraction, Phys. Rev. A **90**, 032710 (2014).

[43] H.-C. Shao and A.F. Starace, Energy-resolved coherent diffraction from laser-driven electronic motion in atoms, Phys. Rev. A **96**, 042706 (2017).

[44] S. Tanaka, V. Chernyak, and S. Mukamel, Time-resolved x-ray spectroscopies: Nonlinear response functions and Liouville-space pathways. Phys. Rev. A **63**, 063405 (2001).

[45] G. Dixit, O. Vendrell, and R. Santra, Imaging electronic quantum motion with light, Proc. Natl. Acad. Sci. USA **109**, 11636 (2012).

[46] A. Kirrander, K. Saita, and D.V. Shalashilin, Ultrafast X-ray Scattering from Molecules, J. Chem. Theory Comput. **12**, 957 (2016).

[47] H.-C. Shao and A.F. Starace, Violation of centrosymmetry in time-resolved coherent x-ray diffraction from rovibrational states of diatomic molecules, Phys. Rev. A **99**, 033413 (2019).

[48] K. Bennett, J.D. Biggs, Y. Zhang, K.E. Dorfman, and S. Mukamel, Time-, frequency-, and wavevector-resolved x-ray diffraction from single molecules, J. Chem. Phys. **140**, 204311 (2014).

[49] M. Simmermacher, N.E. Henriksen, and K.B. Møller, Time-resolved X-ray scattering by electronic wave packets: analytic solutions to the hydrogen atom, Phys. Chem. Chem. Phys. **19**, 19740 (2017).

[50] M. Simmermacher, N.E. Henriksen, K.B. Møller, A.M. Carrascosa, and A. Kirrander, Electronic Coherence in Ultrafast X-Ray Scattering from Molecular Wave Packets, Phys. Rev. Lett. **122**, 073003 (2019).

[51] A. Looijenga-Vos and M.J. Buerger, Space-group determination and diffraction symbols, in *International Tables for Crystallography*, 5th ed., edited by Th. Hahn (Springer, Norwell, MA, 2005), Vol. A, Chap. 3.1, pp. 44-54.

[52] E.U. Condon, Nuclear motions associated with electron transitions in diatomic molecules, Phys. Rev. **32**, 858 (1928).

[53] E. Merzbacher, *Quantum Mechanics, 3rd Ed.* (John Wiley & Sons, Inc., New York, 1998).

[54] F. Pennacchio, G.M. Vanacore, G.F. Mancini, M. Oppermann, R. Jayaraman, P. Musumeci, P. Baum, and F. Carbone, Design and implementation of an optimal laser pulse front tilting scheme for ultrafast electron diffrac-

tion in reflection geometry with high temporal resolution, Struct. Dyn. **4**, 044032 (2017).
[55] D. Ehgerber, A. Ryabov, and P. Baum, Tilted Electron Pulses, Phys. Rev. Lett. **121**, 094801 (2018).
[56] C.C. Marston and G.G. Balint-Kurti, The Fourier grid Hamiltonian method for bound state eigenvalues and eigenfunctions, J. Chem. Phys. **91**, 3571 (1989).
[57] R. A. Bonham and M. Fink, *High Energy Electron Scattering* (Van Nostrand Reinhold, New York, 1974).
[58] J.H. Hubbell, Wm.J. Veigele, E.A. Briggs, R.T. Brown, D.T. Cromer, and R.J. Howerton, Atomic Form Factors, Incoherent Scattering Functions, and Photon Scattering Cross Sections, J. Phys. Chem. Ref. Data **4**, 471 (1975).
[59] C.-C. Shu, K.-J. Yuan, W.-H. Hu, and S.-L. Cong, Field-free molecular orientation with terahertz few-cycle pulses, J. Chem. Phys. **132**, 244311 (2010).
[60] J. Yu, Y. Liu, Q.-Z. Su, and S.-L. Cong, Long-lived field-free molecular orientation driven by modulated few-cycle terahertz pulses, Chem. Phys. **405**, 89 (2012).
[61] S. Wang, H. Li, W. Zhan, and H. Tao, Field-free orientation of LiH molecule induced by two-color femtosecond and terahertz laser pulses, Laser Phys. **29**, 055301 (2019).
[62] J.C. Williamson and A.H. Zewail, Ultrafast Electron Diffraction 4. Molecular Structures and Coherent Dynamics, J. Phys. Chem. **98**, 2766 (1994).
[63] R. Srinivasan, V.A. Lobastov, C.-Y. Ruan, and A.H. Zewail, Ultrafast Electron Diffraction (UED): A New Development for the 4D Determination of Transient Molecular Structure, Helv. Chim. Acta **86**, 1761 (2003).
[64] H. Partridge and S.R. Langhoff, Theoretical treatment of the $X^1\Sigma^+$, $A^1\Sigma^+$, and $B^1\Pi$ states of LiH, J. Chem, Phys. **74**, 2361 (1981).
[65] M.J. Frisch *et al.*, Gaussian 16, Revision A.03, Gaussian, Inc., Wallingford CT (2016).
[66] F.A. Morse and R.B. Bernstein, Velocity Dependence of the Differential Cross Sections for the Scattering of Atomic Beams of K and Cs by Hg, J. Chem. Phys. **37**, 2019 (1962).
[67] R.K.B. Helbing, Transformations and Averaging Processes for Differential Cross-Section Measurements at Thermal Energies, J. Chem. Phys. **48**, 472 (1968).
[68] G.L. Catchen, J. Husain, and R.N. Zare, Scattering kinematics: Transformation of differential cross sections between two moving frames, J. Chem. Phys. **69**, 1737 (1978).
[69] A. Yagishita, Photoelectron angular distributions from single oriented molecules: Past, present and future, J. Electron Spectrosc. Relat. Phenom. **200**, 247 (2015).
[70] K.-J. Yuan and A.D. Bandrauk, Probing Attosecond Electron Coherence in Molecular Charge Migration by Ultrafast X-Ray Photoelectron Imaging, Appl. Sci. **9**, 1941 (2019).
[71] K.-J. Yuan and A.D. Bandrauk, Asymmetry of Molecular Frame Photoelectron Angular Distributions in H_2^+ by Intense Two-Color Attosecond Pulses: Coherent Excitation and Charge Migration Effects, J. Phys. B: At. Mol. Opt. Phys. (2019). http://iopscience.iop.org/10.1088/1361-6455/ab5bac
[72] H. Stapelfelt and T. Seideman, Colloquium: Aligning molecules with strong laser pulses, Rev. Mod. Phys. **75**, 543 (2003).
[73] T. Seideman and H. Stapelfelt, Nonadiabatic alignment pulses. Concepts, theory, and directions, Adv. Atom. Mol. Opt. Phys. **52**, 289 (2005).
[74] Y. Ohshima and H. Hasegawa, Coherent rotational excitation by intense nonresonant laser fields, Int. Rev. Phys. Chem. **29**, 619 (2010).
[75] C.P. Koch, M. Lemeshko, and D. Sugny, Quantum control of molecular rotation, Rev. Mod. Phys. **91**, 035005 (2019).